catalysts

MDPI

Article

Skeletal Nickel Catalyst for the Methanation Reaction Developed by Laser-Engineered Net-Shaping Technology

Kuo Yan [1], Zaiwen Lin [1,*], Xu Li [2], Meng Chen [3,4], Xiaolong Wang [2], Yuren Wang [3,4], Jun Wang [1] and Heng Jiang [3,4,*]

[1] College of Material Science and Chemical Engineering, Harbin Engineering University, Harbin 150001, China; yankuo1234@126.com (K.Y.); zhqw1888@sohu.com (J.W.)
[2] Huaneng Clean Energy Research Institute, Beijing 102209, China; x_li@qny.chng.com.cn (X.L.); xl_wang@qny.chng.com.cn (X.W.)
[3] Key Laboratory of Microgravity, Institute of Mechanics, Chinese Academy of Sciences, Beijing 100190, China; chenmeng@imech.ac.cn (M.C.); yurenwang@imech.ac.cn (Y.W.)
[4] University of Chinese Academy of Sciences, Beijing 100049, China
* Correspondence: linzaiwen@hrbeu.edu.cn (Z.L.); hengjiang@imech.ac.cn (H.J.); Tel.: +86-196611251436 (Z.L.); +86-010-82544107 (H.J.)

Abstract: Here, we report a skeletal nickel catalyst prepared by cumulative processing. The Ni, Al, and CoCrMo multi-component alloys were printed by a dual-powder laser-engineered net-shaping system, and alloy samples with different components were obtained through high-throughput design. After leaching in 5 mol/L NaOH at 40 °C for 2 h, the specific surface area of the catalyst increased with increasing Al content. Increasing the leaching temperature and prolonging the leaching time also effectively increased the specific surface area of the catalyst. After leaching at 80 °C for 12 h, the specific surface area was 42.36 m^2/g. After cleaning and hydrogen-reduction treatment at 400 °C, the catalyst showed high catalytic activity. The highest conversion rate of CO reached 89.56%, and the selectivity of CH_4 remained above 98% for a long time.

Keywords: clean energy; synthetic natural gas; skeleton nickel; 3D print

Citation: Yan, K.; Lin, Z.; Li, X.; Chen, M.; Wang, X.; Wang, Y.; Wang, J.; Jiang, H. Skeletal Nickel Catalyst for the Methanation Reaction Developed by Laser-Engineered Net-Shaping Technology. *Catalysts* **2022**, *12*, 208. https://doi.org/10.3390/catal12020208

Academic Editors: Vincenzo Vaiano and Olga Sacco

Received: 21 January 2022
Accepted: 7 February 2022
Published: 10 February 2022

1. Introduction

Environmental issues are currently among the main challenges faced by mankind, and clean energy is receiving widespread attention. As a type of clean energy, synthetic natural gas (SNG) has attracted much attention, and it is considered to be an effective way to reduce carbon emissions [1,2]. Additionally, obtaining natural gas through coal gasification and methanation can more rationally utilize coal resources and meet the demands of the natural-gas market in coal-rich countries [3,4]. The skeletal nickel-based catalyst developed by Raney [5,6] has a wide range of applications in the field of SNG. It is low-cost and simple to prepare, and it shows a good catalytic effect. Skeletal nickel is mainly made from Ni–Al alloy powders with different compositions, and Al is leached by an alkaline solution to obtain catalyst powders with a high specific surface area. At present, synthesis of SNG is mainly completed in fixed-bed reactors. However, local overheating easily occurs in fixed-bed reactors, and problems, such as the high-pressure drop caused by powder-catalyst filling, limit production of SNG [7–11].

Methods for preparing catalysts include impregnation, co-precipitation, electrophoretic deposition, microwave, sol–gel, and deposition techniques, such as chemical vapor deposition and atomic layer deposition. However, these methods suffer from low loading levels, the uncontrollable distribution of catalytic species, and low mechanical strength. In addition, the catalysts produced by these methods have poor mechanical properties and are prone to vibration, wear, and pollution when the carrier gas flow fluctuates, and they will block the pipeline in severe cases [8,11–13]. Catalyst material coatings are deposited on

metal or ceramic support structures by relatively novel coating techniques, such as thermal spraying and plasma spraying [14,15]. These methods are also limited and can only grow on substrates with simple geometries, which are not applicable to reactors with complex structures. Large-scale reactors manufactured by traditional methods cannot be flexibly modified after completion, and the difficulty of replacing catalysts after failure inevitably leads to high costs, which is detrimental to the development of related industries [16]. In the field of heterogeneous catalysis, there is a need to improve the adaptability of reactor designs by reducing the size of chemical plants and using modular designs to reduce manufacturing and design costs.

Three-dimensional (3D) printing technology has received extensive attention from researchers because of its advantages in the rapid fabrication of complex-shaped parts. Three-dimensional printing technology, which is also known as additive manufacturing technology, is a rapid prototyping technology based on digital model files. Differing from conventional molding methods, 3D printing produces materials with a certain 3D structure by layer-by-layer printing [17]. Catalysts prepared by 3D printing can better control and optimize the product structure, while adjusting the mass- and heat-transfer properties of the material and reducing the bed pressure drop, increasing the service life of the catalyst [18]. In the energy field, there have been a few reports on the preparation of electrodes [19–22] and micro-reactors [23–27] using 3D printing technology. In the current field of 3D printing of catalysts, 3D printing technology is mainly used to fabricate the support structure, and then the active components are deposited on the framework [23,25–27]. Alternatively, 3D printing can be performed by mixing polymer materials with active ingredients, and the catalysts are obtained by high-temperature calcination [18,24]. There have only been a few studies on 3D printing of alloy catalysts, and they have mainly been Raney copper alloys. Albert et al. [28] used the laser metal deposition technique to prepare a Raney copper catalyst with low product selectivity. Wasserscheid et al. [29] prepared Raney copper with an open periodic structure by the selective electron-beam melting technique, which effectively reduced the bed pressure drop.

Research on skeletal nickel alloy catalysts fabricated by 3D printing has not attracted much attention. In this study, the laser-engineered net-shaping (LENS) [30,31] technique with dual powder feeding was used to prepare Ni–Al alloy catalysts (Figure 1). To improve the CO conversion and product selectivity of the catalyst, a certain amount of the CoCrMo alloy was introduced because addition of such transition metals has been proven to improve the catalyst performance [32–35]. Because the types of alloy powders suitable for the LENS process have not been fully clarified, CoCrMo alloys that have a wide range of applications were selected as additives in this study [30,31,36]. We compared the CO conversion and CH_4 selectivity of the Commercial catalyst CRG-S2S (Davy, UK), Ni–Al alloy catalyst, and the catalyst after adding CoCrMo. We also investigated the effect of different Ni/Al powder ratios and different NaOH leaching conditions on the catalyst specific surface area to better understand the characteristics of 3D-printed skeletal nickel catalysts. Related studies have demonstrated that the sub-regional packing of catalysts with different properties is beneficial in solving the problem of localized superheating in fixed-bed reactors [11,13].

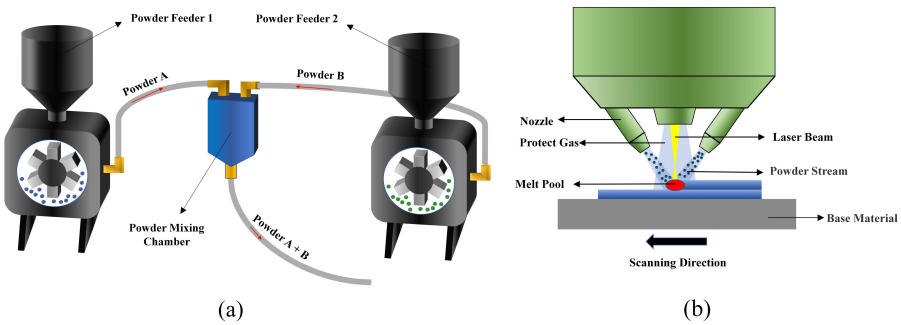

Figure 1. Schematic diagram of the LENS System. (**a**) Working principle of the dual-powder feeder. (**b**) Schematic diagram of the LENS working principle.

2. Experimental Section

All of the samples were prepared by LENS technology. The average diameters of the Ni powder and Al–CoCrMo mixed powder were 45 to 100 μm (Figure 2). The LENS system used a 400 W dual-powder feeder 3D printer. The sample was a sheet with a size of 6 mm × 6 mm and thickness of 1 mm. The process parameters were a laser power of 250 W, scanning speed of 50 cm/min, layer thickness of 25 μm, oxygen content of <20 ppm, and the hatch was set to 75 μm. Printing was performed with different powder feeding speeds (Table 1), and the samples were finally cut using wire electrical discharge machining (WEDM) technology. To test the catalytic activities of different formulations, the samples with different powder ratios were numbered, and the porous catalytic structure was obtained by the alkaline-leaching method.

Figure 2. SEM images of the (**a**) Al power morphology, (**b**) Ni powder morphology, and (**c**) CoCrMo powder morphology.

Table 1. Batch numbers of the samples prepared at different powder feeding speeds.

Batch Number	Powder Feeder Speed (r/min)	
	Ni	Al-CoCrMo
1	2	2
2	2	3
3	2	4
4	3	2
5	4	2

The Al–CoCrMo mixed powder used in 3D printing was a mixture of Al powder and CoCrMo alloy powder. The powder feeder used the LENS system to transport the powder at speeds of 14 and 6 r/min under the no-laser condition. The powder was completely mixed in the mixing chamber before reaching the nozzle, and it was finally sprayed and collected through the nozzle.

Batches 1–5 were added to 5 mol/L NaOH solution and soaked at 40 °C for 2 h. The surface areas of the different batches were determined by the N_2 physisorption method and evaluated by Brunauer–Emmett–Teller (BET). Batch 3 was also leached in 5 mol/L NaOH at different temperatures and for different times (Table 2).

The BET surface area was measured by a surface area analyser (ASAP2460, Micromeritics, Atlanta, GA, USA), and the surface morphology of the sample after leaching was analysed by scanning electron microscopy (SEM) (JEB6510, JEOL, Tokyo, Japan). Batch 3 of the 3D printing powder was analysed by X-ray fluorescence (XRF) spectroscopy (ZSX Primus II, Rigaku, Tokyo, Japan), and the printed flake sample of batch 3 was analysed by SEM/energy dispersive spectroscopy (EDS) (SU8100, Hitachi, Tokyo, Japan) to determine the composition of the 3D printing alloy catalyst.

Table 2. Leaching temperatures and times in 5 mol/L NaOH.

Temperature (°C)	Leaching Time (h)
40	2
40	6
40	12
40	18
20	2
60	2
80	2
80	12

The activity of the catalyst was measured on an adiabatic fixed bed. The catalyst was placed in a stainless-steel reaction tube. Pure hydrogen was fed at a flow rate of 200 mL/min and pressure of 0.1 MPa. The programmed temperature rise rate was 1 °C/min, and a constant temperature reduction was performed at 400 °C for 4 h. The catalyst was then naturally cooled to 240 °C. The pressure was first slowly increased to 3 MPa with nitrogen. The activity was then evaluated under conditions of H_2:CO = 3:1, a H_2 flow rate of 300 mL/min, CO flow rate of 100 mL/min, space velocity of 15,000 h^{-1}, and reaction temperature of 260–280 °C, and the activity data were collected after the evaluation temperature was stable. A gas chromatograph was used to analyse the product (7890B, Agilent, Palo Alto, CA, USA).

3. Results and Discussion

The specific surface areas of the samples with different ratios after alkali leaching were determined by BET analysis. After leaching with an alkali solution at 40 °C for 2 h, the specific surface areas of the samples significantly changed (Figure 3a). After alkali treatment, batch 3 with the highest Al content had the largest specific surface area, whereas batch 5 with the highest nickel content had the smallest specific surface area. Therefore, the Al content directly affected the surface area after alkaline leaching.

For alkaline leaching of batch 3, we found that as the leaching time increased, the specific surface area of the sample significantly increased. After leaching for 18 h, the specific surface area of the sample reached 11.35 m^2/g (Figure 3b). This shows that extending the alkali leaching time can make Al and NaOH more fully react and effectively increase the specific surface area of the sample.

Using batch 3, we increased the alkali leaching temperature. With increasing temperature during alkali leaching, the specific surface area of the processed sample significantly increased. When the treatment temperature was 80 °C, the specific surface area reached 29.33 m^2/g (Figure 3c). Finally, we extended the treatment time to 12 h at 80 °C. There was no obvious bubble formation on the surface of the sample, and the Al element on the surface of the sample was removed. The specific surface area of the sample reached 42.36 m^2/g. This also shows that the Al starts to be severely depleted in the leaching of 2 h, and the dealloying process slows down in the following 10 h. The main reason for this result is that the efficiency of the 3D printed skeleton structure during alkali leaching is lower than that of the powdered skeleton catalyst, and the diffusion efficiency is effectively improved by increasing the temperature during leaching. More severe leaching conditions can promote the performance of the catalyst. With the increase of the leaching temperature and the increase of the leaching time, the specific surface area of the catalyst changes more obviously. The study by Lee et al. showed that more severe leaching conditions have a promoting effect on catalyst activity and CH_4 selectivity [37].

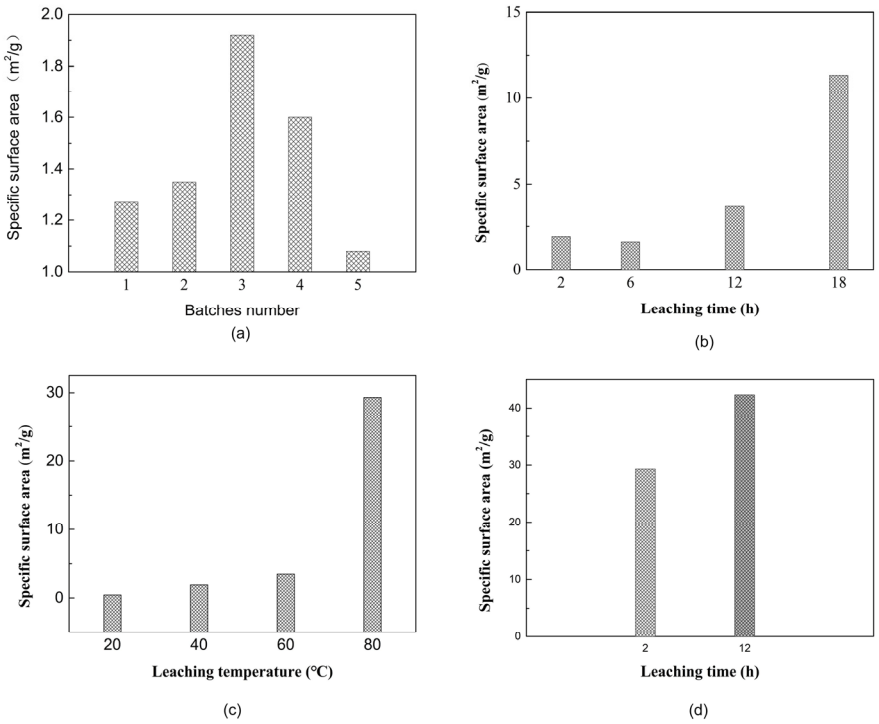

Figure 3. (**a**) Specific surface areas of the different batches leached at 40 °C for 2 h. (**b**) Specific surface areas of batch 3 at 40 °C for leaching times of 2, 6, 12, and 18 h. (**c**) Specific surface areas of batch 3 leached at 20, 40, 60, and 80 °C for 2 h. (**d**) Specific surface areas of batch 3 leached at 80 °C for 2 and 12 h.

After alkali leaching treatment at 40 °C for 2 h, the surface morphologies of the different batches were greatly different (Figure 4). The surface of batch 1 had a large convex structure, and the overall surface was completely filled without obvious gaps (Figure 4a). Batch 2 was prone to granular protrusions, and the overall surface unevenness was different, with a large number of holes (Figure 4b). The surface of batch 3 was composed of petal-like protrusions, with large holes formed on the surface, and there were obvious ravine-shaped stripes (Figure 4c). The size of the convex structure on the surface of batch 4 significantly increased (Figure 4d), and the surface of batch 5 showed densely arranged scales (Figure 4e). The surface structure of batch 3 was more complex and had a larger specific surface area.

After batch 3 was treated by alkali leaching at 60 and 80 °C for 2 h, SEM observation showed that the surface pore density of the sample alkali treated at 80 °C was significantly higher than that of the sample processed at 60 °C (Figure 5b). The sample alkali treated at 80 °C showed obvious spongy structures (Figure 5d) with only thin-walled structures between the pores. This shows that the various powders were uniformly mixed during the preparation of the sample, Al was evenly distributed in the sample, and uniform pores can be formed by alkali leaching treatment.

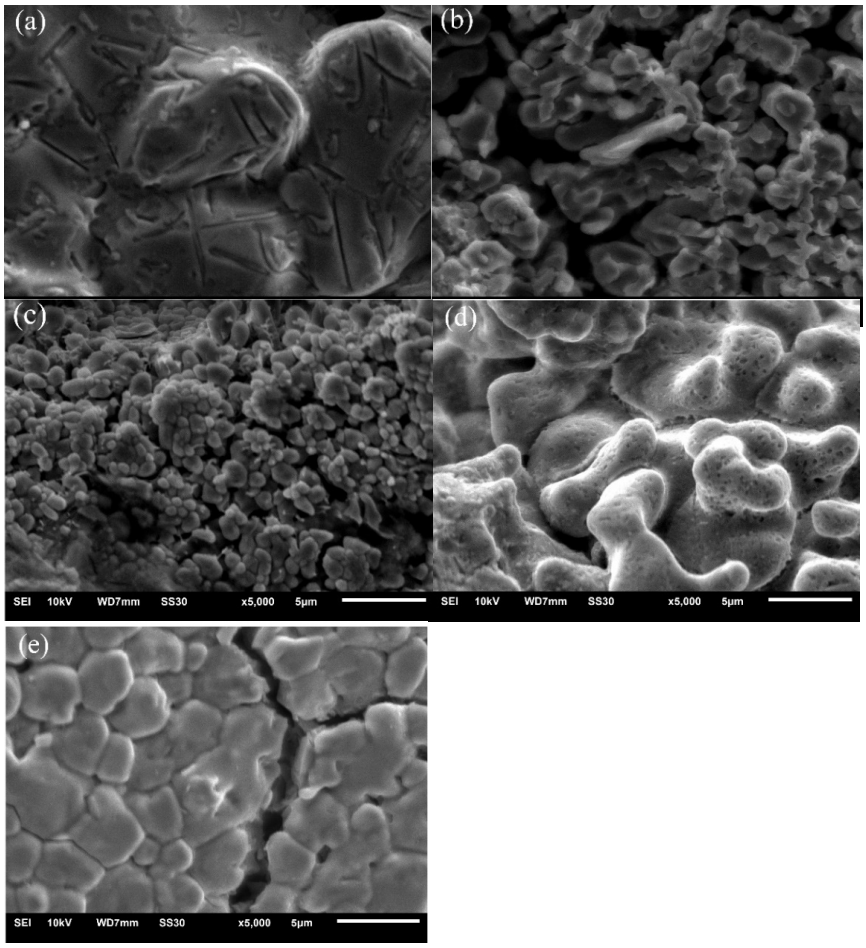

Figure 4. Structures of the different batches soaked in 5 mol/L NaOH solution at 40 °C for 2 h. (**a**) Batch 1 (Ni:Al–CoCrMo = 1:1). (**b**) Batch 2 (Ni:Al–CoCrMo = 1:1.5). (**c**) Batch 3 (Ni:Al–CoCrMo = 1:2). (**d**) Batch 4 (Ni:Al–CoCrMo = 1.5:1). (**e**) Batch 4 (Ni:Al–CoCrMo = 2:1).

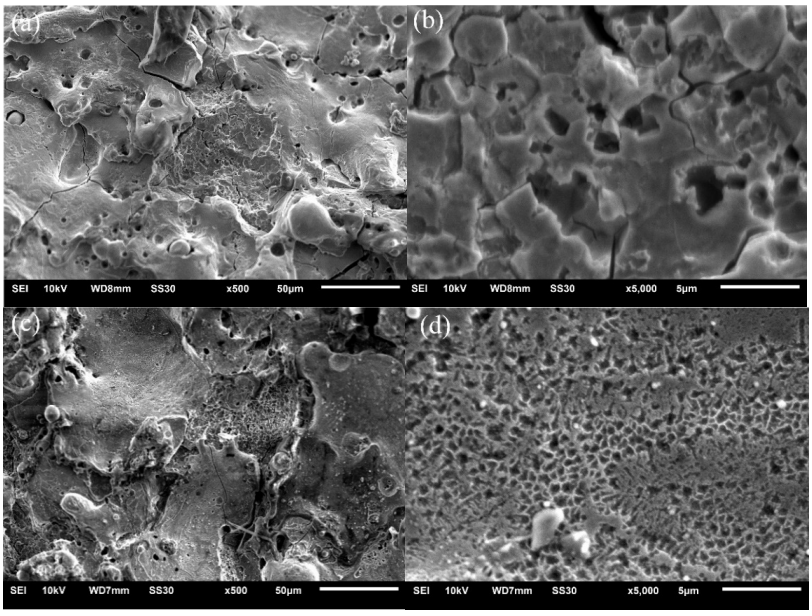

Figure 5. (**a**) Structure of batch 3 after leaching at 60 °C for 2 h. (**b**) Surface pores of the sample after leaching at 60 °C. (**c**) Structure of batch 3 obtained by leaching at 80 °C for 2 h. (**d**) Surface pores of the sample after leaching at 80 °C.

Batch 3 was leached in 5 mol/L NaOH at 40 °C for 6, 12, and 18 h (Figure 6). As the treatment time increased, the size of the surface pores of the alloy also increased. The Al on the surface was continuously dissolved during leaching, gradually exposing the active components. After leaching the alloy at 80 °C for 12 h, there were no obvious air bubbles, a large number of convex structures, and the active components were fully exposed on the surface (Figure 6d).

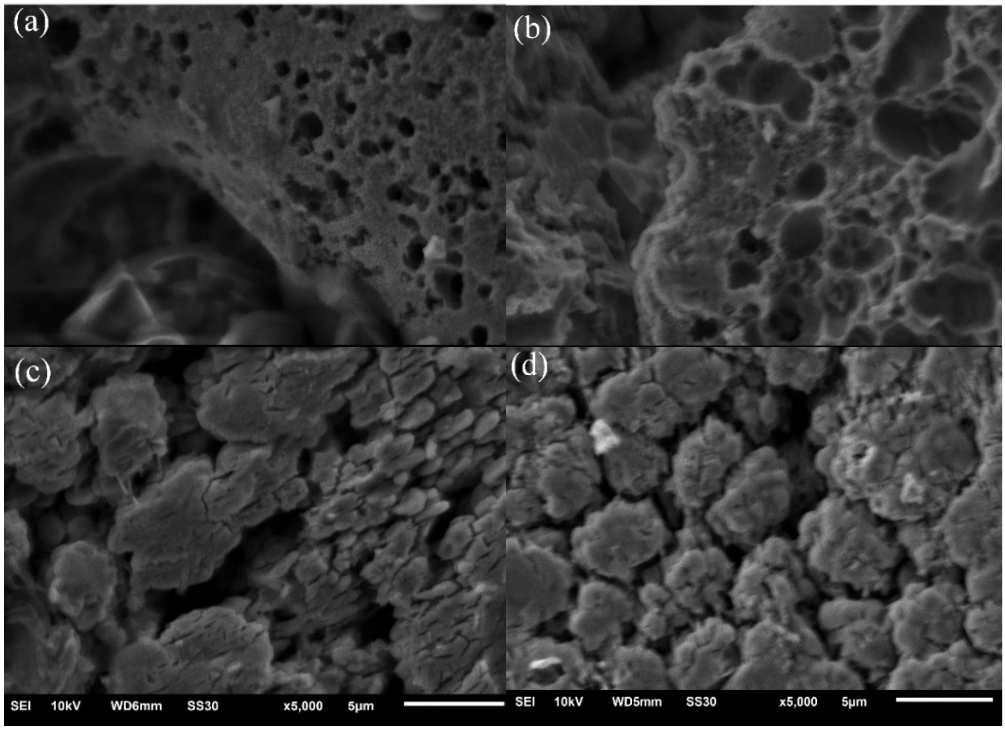

Figure 6. SEM images of batch 3 after leaching in 5 mol/L NaOH at different temperatures for different times. (**a**) 40 °C for 6 h. (**b**) 40 °C for 12 h. (**c**) 40 °C for 18 h. (**d**) 80 °C for 12 h.

After dealloying, a large number of pore structures were produced on the surface of the catalyst, but the overall structure of the catalyst remained good, and the internal structure was intact. This indicates that the alloy catalyst prepared by the 3D printing method can maintain structural integrity. Compared with the impregnation method, this characteristic can take into account the mechanical properties of the catalyst, which can optimise the wear and shedding of the surface layer of the catalyst prepared by the coating method [20]. Preparing monolithic catalysts by the 3D printing method has great advantages in improving the catalyst durability and reducing product contamination.

Actual XRF test results are biased compared to the nominal powder composition. This is due to the presence of impurities in the powder. At the same time, the powder mixed by the powder feeder is partially mixed unevenly. By comparing the XRF (Table 3) and EDS (Figure 7) results of the 3D printing powder and alloy, the mass fraction of each element showed a certain change during the 3D printing process. Among the elements, Al showed obvious mass loss, whereas the mass percentages of the other elements increased. This is because Al has a lower melting point than Ni and CoCrMo alloys. The melting point of Ni (1455 °C) is much higher than that of Al (660.4 °C). During printing, Al vapour is generated instead of staying in the molten pool, which causes a greater loss of Al [31]. In the skeletal nickel catalyst, the loss of Al will greatly affect the specific surface area of the catalyst after dealloying.

Table 3. Element mass percentages of batch 3 determined by XRF analysis.

	XRF	Nominal
Element	**Mass%**	**Mass%**
Al	59.13	64.00
Ni	34.06	32.00
Co	1.87	2.60
Cr	1.49	1.20
Mo	0.46	0.20
others	0.30	-

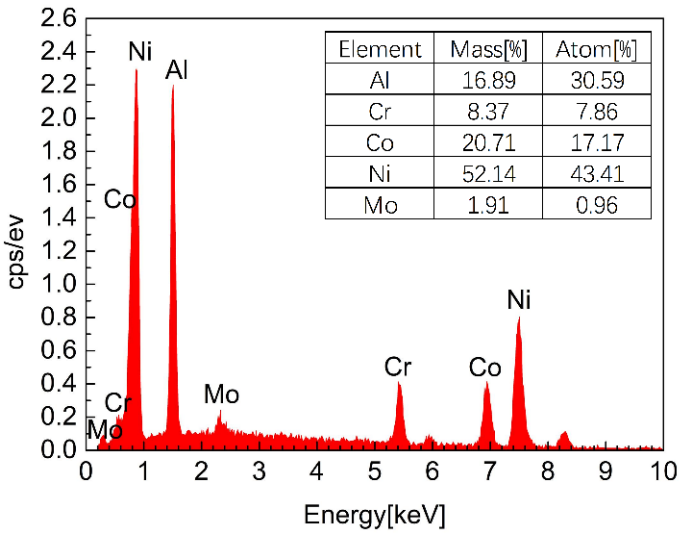

Figure 7. EDS spectrum of batch 3.

The dealloyed catalyst showed reductivity in the H_2-TPR test (Figure 8). With increasing temperature, the H_2 reduction peak reached 570 °C, and NiO was reduced in this range. The second reduction zone appeared between 750 and 850 °C, which is similar to the reduction curve of the Ni/Co catalysts studied by Chen et al. [34], indicating that addition of Co affects the reducibility of Ni catalysts.

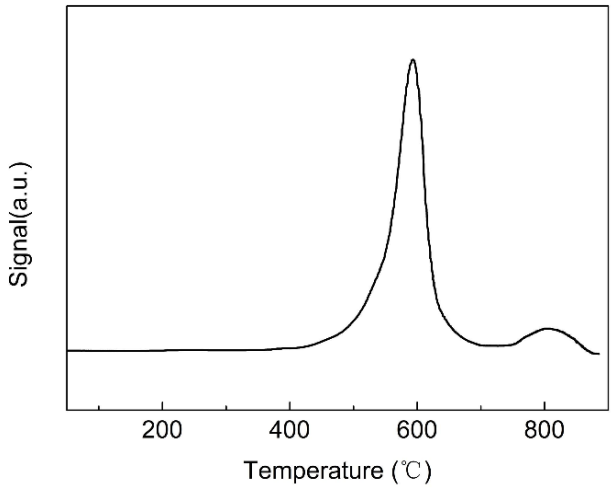

Figure 8. H_2-TPR test results of the alloy catalyst heated at 10 °C min^{-1} with 10% H_2/Ar gas mixture.

Chromatographic analysis of the products showed that the catalyst was activated at 400 °C. When the specific surface of the 1Ni–2Al/CoCrMo alloy catalyst reached

42.36 m^2/g, the reaction started at 260 °C. The CO conversion rate reached 89.54% after 1 h of reaction. It then gradually decreased as the reaction progressed, and the CO conversion rate remained above 60% until 300 min. It decreased to 45.06% at 310 min, and the catalytic activity was significantly lost (Figure 9a). After 250 min, the activity of the catalyst showed a slight increase, which indicated that some of the active sites were reactivated under the action of H_2 as the reaction progressed. The highest CO conversion rate of the pure Ni catalyst was only 47.98%, it remained above 40% from 120 to 340 min, and the CO conversion rate was generally lower than that of the 1Ni–2Al/CoCrMo alloy catalyst (Figure 9a). This indicates that the addition of the CoCrMo alloy is beneficial for the improvement of the CO conversion rate and catalytic efficiency of the Ni catalyst. The CO conversion of the commercial catalyst (CRG-S2S) in the initial stage of the reaction was 39.6%, and with the increase of reaction time, it could reach 89.95% at 260 min and remained stable. The CO conversion rate of the commercial catalyst after stabilization is higher than that of the catalyst prepared by 3D printing technology, which is due to the larger specific surface area, more exposed active sites, and wider distribution of the commercial catalyst [28].

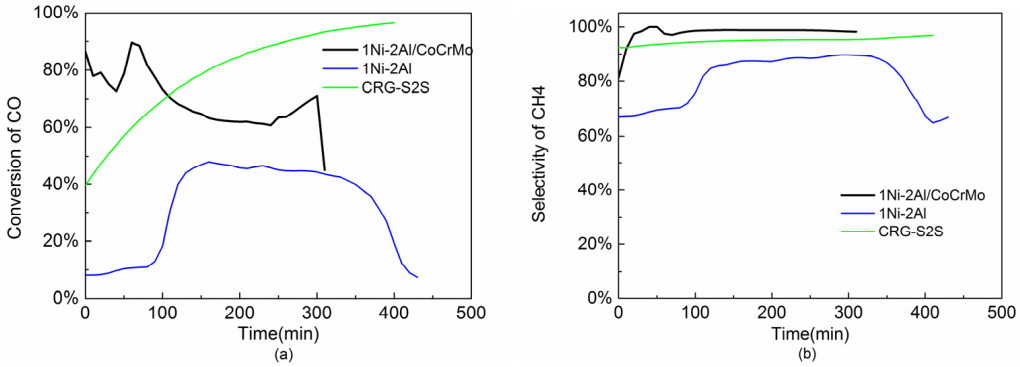

Figure 9. (**a**) Conversion of CO for 310 min. (**b**) Selectivity of CH_4 for 310 min.

As the reaction progressed, the CH_4 selectivity of the 1Ni–2Al/CoCrMo alloy catalyst began to stabilise at 20 min, reached 100% from 40–50 min, and remained above 98% until the end of the reaction (Figure 9b). This shows that the catalyst has good CH_4 selectivity in CO hydrogenation. For the pure 1Ni–2Al alloy, the selectivity of CH_4 was maintained at 80–90% for 110–370 min, and the stability was significantly lower than that of the 1Ni–2Al/CoCrMo alloy catalyst. This may be the result of the multiple effects of the transition metal elements Co and Mo, both of which improve the methane selectivity [33,34]. Compared with the single Ni catalyst, this complex multi-component catalyst can effectively improve the selectivity of CH_4 and inhibit the occurrence of side reactions. However, the catalysts from the LENS process showed a slight improvement in CH_4 selectivity over commercial catalysts, indicating that the multicomponent alloy catalysts have a greater advantage in CH_4 selectivity.

4. Conclusions

In this study, we investigated the possibility of using LENS technology to prepare Ni–Al–CoCrMo alloy catalysts and reached the following conclusions:

1. With increasing Al content, the specific surface area of the alloy after leaching in NaOH solution significantly increased. Increasing the leaching temperature and prolonging the leaching time effectively increased the specific surface area of the catalyst. After leaching with 5 mol/L NaOH at 80 °C for 12 h, the dealloying process was basically complete, and the specific surface area of the catalyst reached 42.36 m^2/g.

2. Through analysis of the composition of the 3D printing powder and alloy, we found that Al mass loss was obvious during the 3D printing process, and the very large difference in the melting points of Ni and Al was the main cause for element loss. The loss of Al seriously affected the specific surface area of the catalyst after dealloying.

3. The activity of the catalyst was the highest at 60 min, and the CO conversion rate reached 89.54%. With time, the conversion rate decreased to around 60%, and the conversion rate significantly decreased after 310 min. Some active sites were activated by H_2 when the reaction progressed to 250 min, and the catalytic performance temporarily improved.

4. During the reaction process of the catalyst, the CH_4 selectivity reached a stable state at 20 min, and it remained above 98% or even 100% for a long time. Addition of the transition metal elements Co and Mo and the composition of the composite catalyst had positive effects on the catalytic performance.

We initially investigated the possibility of using LENS technology to develop a new type of scaffold Ni catalyst. Taking advantage of the unique advantage of the rapid preparation of different component materials, we developed Ni–Al–CoCrMo alloy catalyst preparation technology for methanation synthesis. In addition, the nickel alloy catalyst prepared in this study can be used in the manufacture of the porous honeycomb structure, which provides a new way for the design and production of a new SNG reactor. However, the process parameters and catalyst composition still need to be further improved, and how the problem of Al loss in the preparation process can be solved still needs to be further investigated. At the same time, catalyst deactivation and related research are also issues that need attention. We will consider the effect of carbon deposition and sulphur poisoning on catalyst deactivation in future research. Research on the recyclability of deactivated catalysts and the recovery of spent catalysts will also be our next steps.

Author Contributions: Literature retrieval, K.Y.; chart making, K.Y.; data analysis, K.Y.; manuscript writing, K.Y.; data collection, X.L.; data analysis, M.C., Y.W.; research ideas, X.W., J.W.; revision, H.J., Z.L.; coordination, H.J., Z.L. All authors have read and agreed to the published version of the manuscript.

Funding: The research work was funded by National Natural Science Foundation of China (11972034); the Beijing Research Program (Z171100000817010); the Strategic Pilot Research Program of the Chinese Academy of Sciences (XDB22040301).

Data Availability Statement: The data presented in this study are available.

Conflicts of Interest: The authors declare no conflict of interest.

References

1. Lu, W.; Su, M.; Fath, B.D.; Zhang, M.; Hao, Y. A systematic method of evaluation of the Chinese natural gas supply security. *Appl. Energy* **2016**, *165*, 858–867. [CrossRef]
2. Kopyscinski, J.; Schildhauer, T.J.; Biollaz, S.M.A. Production of synthetic natural gas (SNG) from coal and dry biomass—A technology review from 1950 to 2009. *Fuel* **2010**, *89*, 1763–1783. [CrossRef]
3. Lebarbier, V.M.; Dagle, R.A.; Kovarik, L.; Albrecht, K.O.; Li, X.; Li, L.; Taylor, C.E.; Bao, X.; Wang, Y. Sorption-enhanced synthetic natural gas (SNG) production from syngas: A novel process combining CO methanation, water-gas shift, and CO_2 capture. *Appl. Catal. B: Environ.* **2014**, *144*, 223–232. [CrossRef]
4. Yi, Q.; Wu, G.-S.; Gong, M.-H.; Huang, Y.; Feng, J.; Hao, Y.-H.; Li, W.-Y. A feasibility study for CO_2 recycle assistance with coke oven gas to synthetic natural gas. *Appl. Energy* **2017**, *193*, 149–161. [CrossRef]
5. Raney, M. Catalysts From Alloys. *Ind. Eng. Chem.* **2002**, *32*, 1199–1203. [CrossRef]
6. Covert, L.W.; Adkins, H. Nickel by the Raney Process as a Catalyst of Hydrogenation. *J. Am. Chem. Soc.* **2002**, *54*, 4116–4117. [CrossRef]
7. Lustemberg, P.G.; Ramírez, P.J.; Liu, Z.; Gutiérrez, R.A.; Grinter, D.G.; Carrasco, J.; Senanayake, S.D.; Rodriguez, J.A.; Ganduglia-Pirovano, M.V. Room-Temperature Activation of Methane and Dry Re-forming with CO_2 on Ni-CeO_2(111) Surfaces: Effect of Ce^{3+} Sites and Metal–Support Interactions on C–H Bond Cleavage. *ACS Catal.* **2016**, *6*, 8184–8191. [CrossRef]
8. Theofanidis, S.A.; Galvita, V.V.; Poelman, H.; Marina, G.B. Enhanced carbon-resistant dry reforming Fe-Ni catalyst: Role of Fe. *ACS Catal.* **2015**, *5*, 3028–3039. [CrossRef]
9. Bian, Z.; Suryawinata, I.Y.; Kawi, S. Highly carbon resistant multicore-shell catalyst derived from Ni-Mg phyllosilicate nanotubes@silica for dry reforming of methane. *Appl. Catal. B Environ.* **2016**, *195*, 1–8. [CrossRef]
10. Zhao, Y.; Kang, Y.; Li, H.; Li, H. CO_2 conversion to synthesis gas via DRM on the durable Al2O3/Ni/Al2O3 sandwich catalyst with high activity and stability. *Green Chem.* **2018**, *20*, 2781–2787. [CrossRef]
11. Ding, Y.L.; Wang, Z.L.; Wen, D.S.; Ghadiri, M. Hydrodynamics of gas–solid two-phase mixtures flowing upward through packed beds. *Powder Technol.* **2005**, *153*, 13–22. [CrossRef]
12. Bartholomew, C.H. Mechanisms of catalyst deactivation. *Appl. Catal. A Gen.* **2001**, *212*, 17–60. [CrossRef]

13. Rönsch, S.; Schneider, J.; Matthischke, S.; Schlüter, M.; Götz, M.; Lefebvre, J.; Prabhakaran, P.; Bajohr, S. Review on methanation–From fundamentals to current projects. *Fuel* **2016**, *166*, 276–296. [CrossRef]
14. Wolf, A.; Turek, T.; Mleczko, L. Structured Raney Nickel Catalysts for Liquid-Phase Hydrogenation. *Chem. Eng. Technol.* **2016**, *39*, 1933–1938. [CrossRef]
15. Rashid, M.U.; Daud, W.M.A.W.; Abbas, H.F. Corrigendum to "Dry reforming of methane: Influence of process parameters—A review" [Renew Sustain Energy Rev 45 (2015) 710–744]. *Renew. Sustain. Energy Rev.* **2020**, *133*. [CrossRef]
16. Mardani, S.; Ojala, L.S.; Uusi-Kyyny, P.; Alopaeus, V. Development of a unique modular distillation column using 3D printing. *Chem. Eng. Processing-Process Intensif.* **2016**, *109*, 136–148. [CrossRef]
17. Duda, T.; Raghavan, L.V. 3D Metal Printing Technology. *IFAC-Pap.* **2016**, *49*, 103–110. [CrossRef]
18. Stuecker, J.N.; Miller, J.E.; Ferrizz, R.E.; Mudd, J.E.; Cesarano, J. Advanced Support Structures for Enhanced Catalytic Activity. *Ind. Eng. Chem. Res.* **2004**, *43*, 51–55. [CrossRef]
19. Lacey, S.D.; Kirsch, D.J.; Li, Y.; Morgenstern, J.T.; Zarket, B.C.; Yao, Y.; Dai, J.; Garcia, L.Q.; Liu, B.; Gao, T.; et al. Extrusion-Based 3D Printing of Hierarchically Porous Advanced Battery Electrodes. *Adv. Mater* **2018**, *30*, e1705651. [CrossRef] [PubMed]
20. Ambrosi, A.; Moo, J.G.S.; Pumera, M. Helical 3D-Printed Metal Electrodes as Custom-Shaped 3D Platform for Electrochemical Devices. *Adv. Funct. Mater.* **2016**, *26*, 698–703. [CrossRef]
21. Di Lorenzo, M.; Thomson, A.R.; Schneider, K.; Cameron, P.J.; Ieropoulos, I. A small-scale air-cathode microbial fuel cell for on-line monitoring of water quality. *Biosens Bioelectron* **2014**, *62*, 182–188. [CrossRef] [PubMed]
22. Taylor, A.D.; Kim, E.Y.; Humes, V.P.; Kizuka, J.; Thompson, L.T. Inkjet printing of carbon supported platinum 3-D catalyst layers for use in fuel cells. *J. Power Sources* **2007**, *171*, 101–106. [CrossRef]
23. Chaparro-Garnica, C.Y.; Jorda-Faus, P.; Bailon-Garcia, E.; Ocampo-Perez, R.; Aguilar-Madera, C.G.; Davo-Quinonero, A.; Lozano-Castello, D.; Bueno-Lopez, A. Customizable Heterogeneous Catalysts: Nonchanneled Advanced Monolithic Supports Manufactured by 3D-Printing for Improved Active Phase Coating Performance. *ACS Appl. Mater. Interfaces* **2020**, *12*, 54573–54584. [CrossRef] [PubMed]
24. Fu, Y.; Xu, G.; Chen, Z.; Liu, C.; Wang, D.; Lao, C. Multiple metals doped polymer-derived SiOC ceramics for 3D printing. *Ceram. Int.* **2018**, *44*, 11030–11038. [CrossRef]
25. Danaci, S.; Protasova, L.; Snijkers, F.; Bouwen, W.; Bengaouer, A.; Marty, P. Innovative 3D-manufacture of structured copper supports post-coated with catalytic material for CO_2 methanation. *Chem. Eng. Process.-Process Intensif.* **2018**, *127*, 168–177. [CrossRef]
26. Davo-Quinonero, A.; Sorolla-Rosario, D.; Bailon-Garcia, E.; Lozano-Castello, D.; Bueno-Lopez, A. Improved asymmetrical honeycomb monolith catalyst prepared using a 3D printed template. *J. Hazard. Mater.* **2019**, *368*, 638–643. [CrossRef]
27. Tubío, C.R.; Azuaje, J.; Escalante, L.; Coelho, A.; Guitián, F.; Sotelo, E.; Gil, A. 3D printing of a heterogeneous copper-based catalyst. *J. Catal.* **2016**, *334*, 110–115. [CrossRef]
28. Heßelmann, C.; Wolf, T.; Galgon, F.; Körner, C.; Albert, J.; Wasserscheid, P. Additively manufactured RANEY®-type copper catalyst for methanol synthesis. *Catal. Sci. Technol.* **2020**, *10*, 164–168. [CrossRef]
29. Wolf, T.; Fu, Z.; Ye, J.; Heßelmann, C.; Pistor, J.; Albert, J.; Wasserscheid, P.; Körner, C. Periodic Open Cellular Raney-Copper Catalysts Fabricated via Selective Electron Beam Melting. *Adv. Eng. Mater.* **2020**, *22*. [CrossRef]
30. Li, Y.; Hu, Y.; Cong, W.; Zhi, L.; Guo, Z. Additive manufacturing of alumina using laser engineered net shaping: Effects of deposition variables. *Ceram. Int.* **2017**, *43*, 7768–7775. [CrossRef]
31. DebRoy, T.; Wei, H.L.; Zuback, J.S.; Mukherjee, T.; Elmer, J.W.; Milewski, J.O.; Beese, A.M.; Wilson-Heid, A.; De, A.; Zhang, W. Additive manufacturing of metallic components–Process, structure and properties. *Prog. Mater. Sci.* **2018**, *92*, 112–224. [CrossRef]
32. Zhi, C.; Yang, W. Improvement of Mo-doping on sulfur-poisoning of Ni catalyst: Activity and selectivity to CO methanation. *Comput. Theor. Chem.* **2021**, *1197*. [CrossRef]
33. Bian, Z.; Meng, X.; Tao, M.; Lv, Y.; Xin, Z. Effect of MoO3 on catalytic performance and stability of the SBA-16 supported Ni-catalyst for CO methanation. *Fuel* **2016**, *179*, 193–201. [CrossRef]
34. Cao, K.; Gong, M.; Yang, J.; Cai, J.; Chu, S.; Chen, Z.; Shan, B.; Chen, R. Nickel catalyst with atomically-thin meshed cobalt coating for improved durability in dry reforming of methane. *J. Catal.* **2019**, *373*, 351–360. [CrossRef]
35. Liu, Q.; Zhong, Z.; Gu, F.; Wang, X.; Lu, X.; Li, H.; Xu, G.; Su, F. CO methanation on ordered mesoporous Ni–Cr–Al catalysts: Effects of the catalyst structure and Cr promoter on the catalytic properties. *J. Catal.* **2016**, *337*, 221–232. [CrossRef]
36. Krishna, B.V.; Xue, W.; Bose, S.; Bandyopadhyay, A. Functionally graded Co-Cr-Mo coating on Ti-6Al-4V alloy structures. *Acta Biomater.* **2008**, *4*, 697–706. [CrossRef] [PubMed]
37. Lee, G.D.; Moon, M.J.; Park, J.H.; Park, S.S.; Hong, S.S. Raney Ni Catalysts Derived from Different Alloy Precursors Part II. CO and CO_2 Methanation Activity. *Korean J. Chem. Eng.* **2005**, *22*, 541–546. [CrossRef]